Fluid-flow-induced pattern formation in liquid crystals in a rotating magnetic field

Kalman B. Migler* and Robert B. Meyer
The Martin Fisher School of Physics, Brandeis University, Waltham, Massachusetts 02254
(Received 12 August 1991; revised manuscript received 1 February 1992)

We present a numerical study of pattern formation in the asynchronous regime of a homeotropically aligned nematic liquid crystal under the influence of an in-plane continuously rotating magnetic field. Experimentally, this system has been shown to produce several pattern-forming states. Here, we test the hypothesis that these dynamic patterns exist due to a coupling between spatial gradients in the nematic director and gradients in the fluid flow. We derive the equations of motion coupling the director and hydrodynamic flow from the Leslie-Erickson equations and numerically integrate them in the asynchronous regime. We show that there are two pathways by which a sample that is initially in a homogeneous state can evolve into a dynamic pattern. The first path is through a large external disturbance which nucleates pattern formation and the second is through the amplification of thermal fluctuations, both of which are experimentally observed. We find that the fluid-flow coupling is essential in order to reproduce the experimental behavior. Intuitively, the coupling of the director with the flow creates a lower effective viscosity than in the absence of the flow.

PACS number(s): 61.30.Gd, 61.30.Eb, 47.20.−k

I. INTRODUCTION

A continuous dissipative medium driven away from equilibrium by a uniform external field can respond in a spatially nonuniform manner. Two well-known examples of such behavior are the hydrodynamic instabilities in shear flow or in temperature gradients [1], and pattern formation in a few reaction diffusion systems, such as Belousov-Zhabotinskii [2]. In nematic liquid crystals (NLC's), there are unique experimental realizations of pattern formation, due to the anisotropies of many of its fundamental parameters: viscosities, elastic constants, diamagnetic susceptibility, dielectic permittivity, and conductivities [3].

A key ingredient in many of the liquid-crystal experiments performed to date is the coupling of gradients in fluid flow with gradients in the director field. The best-known example is an electrohydrodynamic instability in which a voltage V is applied between two plates sandwiching a NLC with planar alignment (director aligned along a unique axis parallel to the plates) [4]. When $V > V_c$, for suitable material parameter conditions, a static periodic distortion of the director field is observed. This distorted field is maintained in part by a convective instability. Counter-rotating fluid rolls create a torque on the director which distorts it. In turn, the distorted director field, through an anisotropy in conduction, maintains the flow field. More recently, this class of experiment has been used to study transitions to spatiotemporal turbulence through defect formation and propagation [5].

A second interesting experiment is the instability of the director field of a homeotropically aligned NLC (director perpendicular to the glass plates at the plate boundaries) to elliptical shear flow, discovered by Pieranski and Guyon [6]. They interpret their results as a positive feedback in which convective rolls distort the initial director configuration; the distorted configuration creates bulk forces that amplify the convection.

In the above two examples, the systems are driven continuously away from equilibrium by the externally applied fields. Another class of experiments is transient patterns in a Fréedericksz transition. In a Fréedericksz transition, the director is initially spatially homogeneous with the director orientation defined by the surface alignment (homeotropic or planar). A field (electric or magnetic) is applied which, in the absence of the surface alignment, would reorient the director by $\pi/2$. There is a competition between field and elastic free energy. Above a threshold field value, the static equilibrium state is distorted. The director is reoriented a finite amount in the bulk of the sample while remaining anchored at the surfaces (strong anchoring limit).

The dynamics of the uniform in-plane Fréedericksz transition were studied by Brochard, Pieranski, and Guyon [7]. In the simplest case of a uniform in-plane transition, the director rotation, and hence the director angular velocity, is zero at the plate surfaces and a maximum in the mid-plane. By analyzing the Leslie-Erikson equations, they realized that this effect gives rise to fluid flow (except in the twist case) and furthermore, this flow acts back on the director to create a reduced effective viscosity. In these early papers, the backflow effect was viewed as a substantial quantitative perturbation; the dynamics was qualitatively not greatly changed except for a rescaled viscosity parameter.

It was later discovered that flow can cause qualitatively new physics. Carr found in-plane one-dimensional transient stripes upon suddenly applying a magnetic field in a splay Fréedericksz transition [8]. Guyon, Meyer, and Salan found that these results can be explained through

a viscosity-reduction mechanism [9]. After linearizing the equations of motion, they found that a transient spatially periodic response involving counter-rotating rolls of flow can produce a lower effective viscosity than a uniform in-plane response. They found that the system chooses a wavelength in order to maximize this response rate. Transient effects in a Fréedericksz transition have since been observed in many different geometries in both low-molecular-weight and polymeric NLC's. A summary of these effects is given by Winkler *et al.* [10].

In a previous work by the present authors, we discovered several pattern-forming states in a homeotropically aligned NLC in a rotating magnetic field [11]. By continuously rotating the field, the NLC is maintained away from equilibrium. That work therefore extended the transient-response experiments mentioned above into the domain of continuously driven systems. Through an analysis of the observed director patterns, we concluded that a viscosity-reduction mechanism is an essential component of the pattern-forming states. Further, we hypothesized that this viscosity reduction was a result of a coupling of director gradients and fluid flow, in analogy with the systems previously mentioned. One difficulty of incorporating flow effects into the theoretical analysis is that the distortions are large and the equations are complicated and nonlinear.

In this work, we test the hypothesis that the coupling between director gradients and fluid flow is the driving force behind the pattern formation. Using reasonable approximations, we derive the equations of motion coupling the director and hydrodynamic flow from the Leslie-Erickson equations and numerically integrate them in the asynchronous regime. We show that there are two pathways in which a sample that is initially in a homogeneous state can evolve into a dynamic pattern. The first path is through a large external disturbance which nucleates pattern formation; experimentally this is observed in the pattern that we call the *viscosity-reduction lattice*. The second is through the amplification of thermal fluctuations; this amplification is observed to occur in the early stages of what we call the *complex* state. Depending on the values of the field strength and sample rotation rate, both pathways to pattern formation are experimentally observed.

The outline of this paper is the following: in Sec. II, we describe the basic experiment, and review the theory for the dynamics in which there is no pattern formation. In Sec. III, the experimental pattern-forming states are reviewed. In Sec. IV, we derive the equations of motion incorporating fluid flow based on certain physically reasonable approximations. In Sec. V, we discuss the viscosity-reduction lattice (VRL). A VRL is nucleated in an initially homogeneous sample by a local disturbance that creates a local increase in effective rotational viscosity. Through fluid-coupling effects, a lattice is formed that has a lower effective viscosity than the uniform in-plane state. We present the numerical solutions of the Leslie-Erikson equations which confirm the above picture. In Sec. VI, we discuss the amplification of thermal fluctuations by the director-flow coupling and argue that this is responsible for the *complex* state, in which an initially homogeneous state becomes spontaneously disordered.

II. UNIFORM DYNAMIC STATES

The geometry of the experiment is a layer of NLC of thickness d, contained between parallel glass plates at which the director is homeotropically aligned (perpendicular to the glass). The director $\hat{n}$ is described by the usual polar angles (θ, ϕ). A homogeneous magnetic field of strength H, parallel to the x-y plane, rotates with angular frequency ω about the z axis. (See Fig. 1.)

In order to understand the patterns that can form, we must first understand the state that is homogeneous in the x-y plane. Brochard, Léger, and Meyer (BLM) studied the case of a homeotropic nematic liquid crystal in a rotating magnetic field [12,13]. There are three fundamental states called synchronous, asynchronous, and undistorted which can be understood by considering the relative strengths of the elastic, viscous, and magnetic torques that act on the director.

Consider first the limiting case of $\omega = 0$. This is simply the static Fréedericksz transition discussed in the Introduction. The Fréedericksz transition occurs at field strength (in cgs notation):

$$H_{c0} = H_c(\omega = 0) = \frac{\pi}{d}\sqrt{\frac{K_3}{\chi_a}}, \tag{2.1}$$

in which K_3 is the Frank elastic constant for bend, χ_a the magnitude of the anisotropy of the diamagnetic susceptibility, and d the thickness of the sample. Note the degeneracy of the director for $H > H_{c0}$ in that both $\phi = 0$ and $\phi = \pi$ are allowed. Unless one orientation is somehow suppressed, the sample typically forms into random domains of opposite orientations separated by walls.

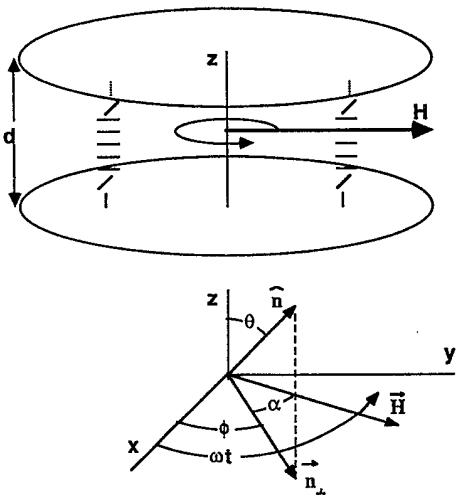

FIG. 1. The geometry of the experiment is a homeotropic nematic-liquid-crystal sample between glass plates in the presence of an in-plane rotating magnetic field.

Now we consider the torque equations for the director in a rotating magnetic field in which the sample is homogeneous in the x-y plane:

$$\gamma_1 \frac{\partial \phi}{\partial t} = \frac{1}{2}\chi_a H^2 \sin[2(\omega t - \phi)], \tag{2.2}$$

$$\gamma_1 \frac{\partial \theta}{\partial t} = \chi_a H^2 \cos^2(\omega t - \phi)\sin\theta\cos\theta + K\frac{\partial^2 \theta}{\partial z^2}, \tag{2.3}$$

using the approximation $K = K_1 = K_3$ in which K_1 is the splay elastic constant, and γ_1 is the rotational viscosity.

The magnetic coherence length

$$l_c = \frac{1}{H}\sqrt{\frac{K_3}{\chi_a}} \tag{2.4}$$

defines a characteristic length over which the director can vary. For fields just over the Fréedericksz transition, $l_c \approx d$, while for fields $H \gg H_{c0}$, l_c defines the width of a boundary layer in which the director varies from $\theta = 0$ at the glass plates to $\theta \approx \pi/2$ in the bulk.

For large H, fluid flow in the homogeneous structure is confined to these boundary regions, subject of course to the constraint that it vanish at $z = \pm d/2$. At high fields these flow regions are much thinner than the sample thickness and are expected to have little impact on the bulk dynamics. The rotational viscosity used above, γ_1, is rescaled by the fluid flow [13,14]. The direction of the flow is perpendicular to the plane defined by (z, n). Fluid flow becomes much more important in pattern-forming regimes.

Note the basic reason for our use of homeotropic boundary conditions: while the director in the mid-region rotates about the z axis, the boundary layers in which the director remains perpendicular to the glass act as pivot or slip surfaces for the director.

The torque equations are simplified by the fact that Eq. (2.2) is independent of θ. Assuming that $H(\omega)$ is strong enough so that there is a Fréedericksz transition, the synchronous regime is defined by the condition that

$$\omega\tau < 1, \tag{2.5}$$

in which

$$\tau = \frac{2\gamma_1}{\chi_a H^2}. \tag{2.6}$$

τ is a characteristic time for the director to rotate in response to the magnetic torque. Equation (2.2) is easily solved in this regime and the solution is independent of time when written in terms of α:

$$\sin(2\alpha) = \omega\tau, \tag{2.7}$$

using

$$\alpha = \omega t - \phi. \tag{2.8}$$

α is the phase-lag angle between $\mathbf{H}$ and the projection of $\hat{n}$ in the x-y plane, $\mathbf{n}_\perp$. (See Fig. 1.)

Thus in the synchronous regime, the director rotates at the same frequency as the field, but lags behind by a constant phase angle α. Since α is constant in time in the synchronous regime, θ is also independent of time via Eq. (2.3). The maximum constant phase-lag angle in the synchronous regime is $\pi/4$ at which point $\omega\tau = 1$ and the magnetic torque about the z axis is a maximum.

The transition between the synchronous and asynchronous regimes occurs at $\omega\tau = 1$ and $H_a(\omega)$ denotes the corresponding magnetic-field strength. If $\omega\tau > 1$ and $H > H_c(\omega)$, then the asynchronous state appears. In this state the rotational viscosity prevents the director from synchronously following the rotation of the field and the phase-lag angle α increases monotonically with time. Also, θ becomes time dependent. In the asynchronous regime BLM found the behavior of α to be

$$\tan\alpha(t) = \frac{1}{\omega\tau} + \left(1 - \frac{1}{(\omega\tau)^2}\right)^{\frac{1}{2}} \times \tan\left(\frac{t}{\tau}(\omega^2\tau^2 - 1)^{\frac{1}{2}} + \phi_0\right). \tag{2.9}$$

The period T is defined as the time for α to increase by π:

$$T = \frac{\pi\tau}{(\omega^2\tau^2 - 1)^{1/2}}. \tag{2.10}$$

Throughout this paper, we will refer to both ϕ and α, depending on which is more convenient. In Fig. 2, both ϕ and α are plotted as a function of time in the asynchronous regime using Eq. (2.9) with $\omega\tau = 1.2$. Whereas ϕ is a linearly increasing function of time in the synchronous regime, here it slows down and reverses direction in what we call the phase-slipping portion of the cycle, i.e., when $\pi/4 < \alpha < 3\pi/4$. For the case of $\omega\tau \approx 1.2$ (Fig. 2), the mean slopes of α and ϕ versus time are approximately equal. This is not true in general; for example in the limit of $\omega\tau \to \infty$, the mean value of $\partial\phi/\partial t \to 0$ while that of $\partial\alpha/\partial t \to \omega$. This is because when $\omega\tau \to \infty$, the magnetic-field rotation rate is much faster than the nematic response rate; thus the director is essentially motionless as the field rotates.

The threshold field $H_c(\omega)$ for the Fréedericksz transition from the undistorted into the synchronous regime can be found by noting that the situation is similar to the stationary Fréedericksz transition except that H is replaced by $H\cos\alpha$. This gives

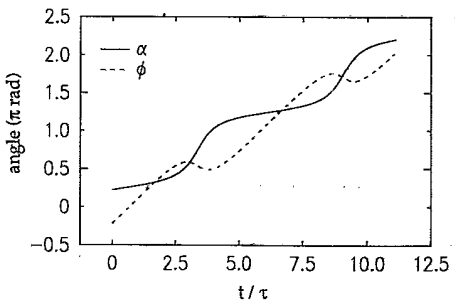

FIG. 2. Solution of Eq. (9), showing a comparison of the behavior of ϕ and α in the asynchronous regime for $\omega\tau = 1.2$

$$H_c^2(\omega) = H_{c0}^2\left(1+\frac{\omega^2}{\omega_1^2}\right), \tag{2.11}$$

in which

$$\omega_1 = \frac{K_3\pi^2}{\gamma_1 d^2} \tag{2.12}$$

defines a characteristic inverse time for $\hat{n}$ to relax to $\theta = 0$ in the absence of a magnetic field. When $\omega > \omega_1$, the Fréedericksz transition occurs into the asynchronous regime at a field [14,15].

$$H_c = \sqrt{2}H_{c0}. \tag{2.13}$$

For what range of external variables is the uniform (i.e., homogeneous in the x-y plane) response stable? Sagués theoretically studied pattern formation associated with the Fréedericksz transition in this geometry and found that in the small-θ approximation, one expects a homogeneous in-plane response, in agreement with experiment for low fields [14]. Also in two limits of $\omega\tau$, we can show that pattern formation is not expected. First consider the limit of $\omega\tau \to 0$. This is the static Fréedericksz transition limit, which was discussed previously. The torque about the z direction, which is essential for pattern formation, goes to zero. In the opposite extreme of $\omega\tau \to \infty$, the physical picture is that the rotation rate is so great compared to the field strength, that ϕ becomes constant in time (or equivalently that α is linearly increasing in time). BLM make the analogy between the $\omega\tau \to \infty$ limit and an electric-field Fréedericksz transition with a negative dielectric anisotropy. Here, the time-averaged torque in the z direction is zero. In these two limits, the uniform description is valid. In the remainder of the paper, we will focus on the case of $\omega\tau$ greater than, but close to 1, and pattern formation is observed.

III. EXPERIMENTAL PATTERN-FORMING STATES

Migler and Meyer studied the case in which the director is spatially nonuniform in the plane of the sample and dynamic pattern formation is observed [11]. Figure 3

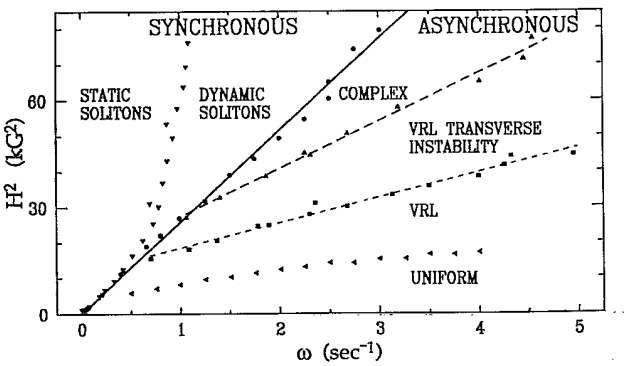

FIG. 3. Experimental pattern-forming-state diagram. The solid line delineates the synchronous-asynchronous transition.

shows the experimentally determined pattern-forming states for a sample thickness of $d = 75$ μm. The diagram is in the limit $H^2 \gg H_{c0}^2$ and $\omega \gg \omega_1$. Therefore the triple point, where the synchronous, asynchronous, and undistorted states coincide, is located in the very lower left portion of the figure (not shown). Also the undistorted state is not explicitly shown because it runs along the very bottom of this figure. The term *uniform* is defined to describe the dynamics of the state in which the director is uniform in the x-y plane, while varying in the z direction. This experimental state diagram supports the earlier statements that a uniform response is stable in the limits of large and small $\omega\tau$ and also in the limit of H only slightly greater than $H_c(\omega)$.

In the synchronous regime, dynamic solitons, also called walls or kinks, were observed. A soliton is a wall-like structure that separates two regions of space differing in the angle of the director by π. The director smoothly varies from α_0 on one side to $\alpha_0 \pm \pi$ on the other. An isolated soliton conserves its shape as it propagates through the sample (neglecting line tension effects). In an initially homogeneous sample, a dynamic soliton can nucleate off of either a dust particle (in which case it propagates outward in a growing ring), or the outer side boundary of the sample, in which case it moves inwards in a shrinking ring. In view of the one-dimensional work that we will present later, we focus on the case of a straight (one-dimensional) outer boundary. In order to understand the stability and propagation of these structures, Eq. (2.2) was generalized to include the elastic torque term $K\partial^2\alpha/\partial x^2$, which describes in-plane spatial nonuniformity in the director field [11]. (This can be further generalized to two dimensions.) This equation has been studied previously [16], and its solution contains stable propagating solitons of amplitude π which are very similar to those observed experimentally.

Physically, nucleation by an outer side boundary occurs because the nucleation site acts locally as a region of enhanced viscosity, inhibiting the rotation of the director. The angle α between the director and the magnetic field increases near this disturbance relative to the bulk of the sample, creating an elastic distortion. Nucleation occurs when this distortion becomes too great; the director at the disturbance phase slips relative to the magnetic field by π, creating a soliton of amplitude π. As this soliton propagates away, the disturbance can nucleate another, and so on, leading to the formation of what we call a lattice of solitons. At a given point in time, α is a *decreasing* function of distance from the sidewall. The average rotation rate within a dynamic soliton lattice is slower than it is in a homogeneous (soliton-free) part of the sample because the net effect of a soliton passing through a point in space is that the director falls behind the rotating field by an amount π.

In the asynchronous regime, the motion of the director even in the absence of pattern formation is rather nontrivial. Thus the challenge of describing and understanding pattern formation in this regime is great. Figure 3 shows four observed states in the asynchronous regime as a function of H and ω: the uniform, the viscosity-reduction lattice (VRL), the VRL transverse instability,

and the *complex* states. The three pattern-forming states are classified by two criteria: First, the mechanism by which an initially homogeneous sample evolves into the final dynamic state and second, the observed final dynamic pattern of the director.

The experimental procedure that was used to study the mechanism by which an initially homogeneous sample evolves into a pattern is the following: The sample was initially placed into the magnetic field of strength H, in the absence of rotation, in such a way as to induce a uniform Fréedericksz transition. In other words, we create a single-domain sample (no walls) in which the director angle is independent of x and y, depending on z in the usual way for a Fréedericksz transition. Then the rotation is quickly turned on, and one observes if and how pattern formation in the x-y plane evolves from the homogeneous sample. We have observed two distinct paths: nucleation-induced pattern formation and spontaneous pattern formation.

We begin the discussion of asynchronous patterns by describing a nucleated pattern: the VRL. Given an initially homogeneous sample and setting H and ω within the VRL part of the state diagram (Fig. 3), one observes a dynamic pattern-forming structure nucleating off of dust particles and the outer-side boundaries. Figure 4 shows a photograph of a VRL that has nucleated off of a sidewall. These structures grow into, and at the expense of, the homogeneous parts of the sample, until they fill the entire sample. An important point is that when H and ω are in the VRL part of the state diagram, an initially homogeneous region of the sample is metastable, rather than unstable, with respect to a VRL. For example, in the case of a dust-particle-nucleated VRL, it is sometimes observed that the center of the VRL slowly drifts away from the dust particle, without affecting the dynamics of the VRL. Thus the dust particle is necessary to initiate pattern formation, but once a pattern is formed, the nucleation site plays little role in the subsequent dynamics. (Note that this is in complete contrast to the dynamic soliton lattice discussed previously in which the external disturbance plays a crucial role in creating each individual soliton.) In the VRL part of the state diagram, small-scale distortions in an initially homogeneous sample increase the elastic energy and are damped out by the counteracting elastic torque. However, when a distortion reaches a critical size, it grows.

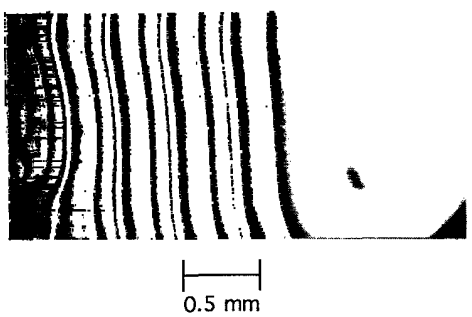

FIG. 4. Photograph of a VRL that has been nucleated from a sidewall and is growing into an initially homogeneous sample. The nematic liquid crystal is birefringent and the sample is sandwiched between crossed polarizers. Thus the intensity of transmitted light gives information about the local orientation of the director.

The most important property of a VRL, in terms of understanding its dynamics, is that the average rotation rate of the director within a VRL is *faster* than the average rotation rate within a homogeneous part of the sample. Equivalently, α is an *increasing* function of distance from the sidewall (in the case that the sidewall is the nucleation source). This is opposite to the dynamic solitons in which α is a decreasing function of distance from the nucleation source. It was this observation that led to the conclusion that there is an apparent reduction in the viscosity in a VRL relative to a homogeneous part of the sample. What is the source of this reduction in apparent viscosity? In analogy with some of the previous experiments in liquid-crystal dynamics, we hypothesized that there is a coupling between director gradients and fluid flow.

The VRL has other interesting dynamic properties. Since the photograph in Fig. 4 is taken through crossed polarizers, the angle α increases by π in the distance between every other black stripe. We call this distance the local wavelength. As the magnetic field rotates, the local structure of the VRL undergoes a rather complex undulation. A second photograph taken when the field has rotated by (say) $\pi/4$ would show a similar structure, but on closer examination would reveal that the various widths of the bright and dark regions that make up a wavelength have changed, although the wavelength itself remains unchanged. The frequency of this undulation is ω, thus a third photograph of the structure taken after the field has rotated one full turn would show a pattern identical to the first but shifted, showing that it has grown slightly into the homogeneous part of the sample.

Nucleation of a viscosity-reduction lattice by a dust particle or outer sidewall, which locally increases viscous drag, sounds like a contradiction. However, our picture of the nucleation process is the following: A sidewall creates a region of increased viscous drag, causing the director to locally rotate more slowly than in the bulk. This results in a distortion in the director field, since α is greater near the nucleation source than in the bulk. Fluid flow is induced by the director gradients. Gradients in the fluid flow then act back on the director, in such a way as to increase the average rotation rate. In the mature VRL, gradients in fluid flow and in the director couple to each other in such a way as to reduce the effective viscosity. The major purpose of the numerical simulations in the remaining sections is to test whether this idea is correct.

The dependence of the wavelength of the VRL on H and ω shows interesting features. As the experimental conditions are moved closer to the uniform state by decreasing H, there is a dramatic increase in the wavelength, diverging at the transition between the two states. At the same time, the rate of growth of the lattice slows down dramatically. It seems that the viscosity-reduction effect is much weaker at the boundary between the VRL and uniform states than at the boundary between the VRL and VRL transverse instability states.

The VRL transverse instability state is similar to the VRL just described in that the nucleation process is similar. However, the appearance of the final dynamic pattern is different in that there is a small amplitude distortion with the wave vector in the direction parallel to the stripes [11]. We shall not pursue this state further as the patterns are inherently two dimensional, while the numerical results that we present are only one dimensional.

In contrast to the VRL and to the VRL transverse instability, in the *complex* region of the state diagram, an initially homogeneous sample is unstable. By this we mean that turning on the rotation of the magnetic field causes spontaneous pattern formation throughout the sample, without the need for nucleation at dust particles or side boundaries. Experimentally, the following sequence is observed: In the first period of the homogeneous cycle when α_{av} begins to phase slip at $\alpha_{av} \approx \pi/4$, stripes perpendicular to the director spontaneously grow throughout the sample, reach a maximum amplitude, and begin to disappear when $\alpha_{av} \approx 3\pi/4$. [The quantity α_{av} refers to the spatial average of $\alpha(x)$ at a given time.] The orientation of the stripes is roughly constant during the above cycle. During the next phase-slip cycle of the director, stripes reappear in a similar manner, but the orientation is different than the previous cycle because the director in general will have a different orientation when the next phase slip occurs. However, one can optically detect some memory of the initial stripes. Thus the stripes from one cycle interact with those from the previous cycle. After a few such cycles, the system becomes increasingly disordered, and large-scale ($> \pi$) inhomogeneities in the director begin to appear.

As time evolves, the pattern gradually becomes organized into a disordered array of local concentric circle patterns, very similar to VRL's nucleated by dust particles. Even this pattern is somewhat transient. A dynamic soliton lattice of much shorter wavelength than the VRL (similar to that seen in the synchronous regime) still nucleates from the sidewall. It competes with the complex state, and at very long times, depending on the exact position in the state diagram, it becomes the dominant pattern. We will not discuss this dynamic soliton lattice structure further in this paper. Note also that VRL-type structures are not nucleated from dust particles or the outer sidewall in the *complex* region of the state diagram. Presumably this nucleation process has been superseded by the homogeneous instability producing the complex state.

In our study of the *complex* state, we will focus on the initial appearance of the transient stripes, as they are approximately one-dimensional and hence may be studied in a one dimensional simulation. In fact, these transient stripes are also observed in a homogeneous portion of a sample in which H and ω are set to be within the VRL or VRL transverse instability states. Here, however, the amplitude of the stripes remains quite small and the stripes have little or no effect on the dynamics of a VRL. Between phase-slip cycles, they die out, implying that this homogeneous state is stable against these small perturbations. As one moves the experimental conditions closer to the *complex* state (say by increasing H), the amplitude of the stripes in a homogeneous part of the sample begins to grow. Finally, when one crosses the boundary into the *complex* state, the stripes are large enough to create pattern formation with large-scale inhomogeneities.

We proposed that these stripes are an amplification of thermal fluctuations and that the mechanism is again a coupling between fluid flow and director gradients. Apparently, only for $\omega\tau$ greater than but close to 1 are these stripes able to grow significantly. In our numerical work, we will examine both the flow fields and the director fields to check that the proposed coupling can also be applied to the case of transient stripes.

IV. HYDRODYNAMIC EQUATIONS

In order to test the idea of pattern formation induced by a coupling between director gradients and fluid flow, we examine the equations of motion for the nematic fluid. We use the Leslie-Erickson equations [4] which contain the coupling that interests us. As these equations are quite complicated, we immediately make physically reasonable approximations in order to eliminate some terms.

In this approach we take the limit $H'^2 \gg 1$ and $\omega' \gg 1$, introducing two dimensionless variables;

$$H' = H/(H_{c0}2^{1/2}) \tag{4.1}$$

and

$$\omega' = \omega/\omega_1. \tag{4.2}$$

This is a reasonable limit since Fig. 3 shows that the *complex state* is in this limit and the VRL state approaches it. Large H'^2 and large ω' means that the large-angle approximation $\theta = \pi/2$ must be used. This is the opposite limit to that used by Sagués [14].

Also, we simplify things by considering one-dimensional pattern formation. Figure 4 shows that this is reasonable. In fact if the outer boundary of this sample were straight, instead of circular, the lines of constant director angle would appear even straighter. We will consider director gradients along the x axis only (perpendicular to the stripes), which couple to fluid flow that is in the y direction (parallel to the stripes). Gradients in the fluid flow are considered in both the x and z directions. There is an important finite-thickness effect associated with the fact that fluid flow goes to 0 at $z = \pm d/2$. Flow generated along a line, say $x = x_o$, decays in a characteristic spatial length $\delta x \approx d$. In order to incorporate this effect, we make a parabolic approximation for the z dependence of the flow field:

$$v_f(x,z,t) = v_{f0}(x,t)\left[1 - \left(\frac{2z}{d}\right)^2\right]. \tag{4.3}$$

We also neglect the variation of θ at the sample boundaries and any variation of ϕ with z. We use the one-constant approximation $K = K_1 = K_3$. These approximations are similar to those in previous works on tran-

sient dynamics [10].

There are two fundamental variables $\omega\tau$ and d, which can be expressed in terms of the more experimentally relevant variables H' and ω':

$$H' = \frac{d'}{\pi} \tag{4.4}$$

and

$$\omega' = \frac{d'^2\omega\tau}{\pi^2}, \tag{4.5}$$

where $d' = d/(l_c 2^{1/2})$ is a dimensionless thickness.

The general expression for the viscous contribution to the torque equation is given by

$$\Gamma_z = n_x h_y - n_y h_x, \tag{4.6}$$

in which h_μ is the viscous contribution to the molecular field:

$$h_\mu = \gamma_1 N_\mu + \gamma_2 n_\alpha A_{\alpha\mu}, \tag{4.7}$$

and

$$A_{\alpha\beta} = \frac{1}{2}(\partial_\alpha v_\beta + \partial_\beta v_\alpha) \tag{4.8}$$

is the symmetric part of the velocity gradient tensor. N_i is the rate of change of the director with respect to the fluid. The viscosity γ_2 is associated with shear flow and is a negative quantity. Using the above approximations the resulting full torque equation is the generalization of Eq. (2.2) with the inclusion of an elastic term due to director gradients and a $\partial_x v_f$ term due to coupling with flow gradients:

$$\gamma_1 \frac{\partial\phi}{\partial t} = K\frac{\partial^2\phi}{\partial x^2} + \frac{1}{2}\chi_a H^2 \sin[2(\omega t - \phi)] - \frac{\partial v_f}{\partial x}(\alpha_2 \cos^2\phi - \alpha_3 \sin^2\phi). \tag{4.9}$$

For the hydrodynamic flow equation, we neglect the inertial term, as is commonly done, because its contribution is negligible:

$$\rho\frac{d}{dt}v_{f\beta} = \partial_\alpha \sigma_{\alpha\beta} = 0, \tag{4.10}$$

in which $\sigma_{\alpha\beta}$ is the general stress tensor. Using the symmetries of our geometry, many terms of the above equation do not contribute. For example, terms involving pressure gradients are absent since this system is invariant in the y direction. We can use the simpler expression

$$\partial_\alpha \sigma'_{\alpha\beta} = 0, \tag{4.11}$$

where $\sigma'_{\alpha\beta}$ is called the viscous stress and is defined in the standard manner [4]. From the previous equation and our approximations we derive

$$0 = \left(\frac{\partial^2 v_{f0}}{\partial x^2}\right)[\eta_c + \gamma_2 \sin^2\phi + \alpha_1(\sin\phi\cos\phi)^2] + \left(\frac{\partial v_{f0}}{\partial x}\frac{\partial\phi}{\partial x}\right)[\gamma_2 \sin(2\phi) + \frac{1}{2}\alpha_1 \sin(4\phi)] + \left(\frac{\partial^2\phi}{\partial x \partial t}\right)(\alpha_2 \cos^2\phi - \alpha_3 \sin^2\phi) - \left(\frac{\partial\phi}{\partial x}\frac{\partial\phi}{\partial t}\right)\gamma_2 \sin(2\phi) + \left(\frac{\partial^2 v_f}{\partial z^2}\right)(\eta_a \cos^2\phi + \eta_b \sin^2\phi). \tag{4.12}$$

The α_i terms are the Leslie viscosity coefficients. The η_i terms are linear combinations of the α_i expressing effective viscosities in simple shear geometries [4]. Equation (4.3) is used in the last term to evaluate the derivative. In the limit $\phi \ll 1$, the above equation reduces to that found by Lonberg *et al.* in the linearized treatment of the twist Fréedericksz transition [17].

The boundary conditions are $\partial_x\phi = 0$ and $v_f = 0$ at the left and right ends. The initial conditions at t'_{in} are $v'_f(x, t'_{\text{in}}) = 0$ and $\phi(x, t'_{\text{in}})$ depends on which pattern-forming state we are examining. Since we are interested in long-time dynamics, the initial v_f is not critical; it quickly adjusts into a dynamic nonhomogeneous value. Equations (4.9) and (4.12) were solved through numerical integration on a grid using a method similar to Srajer, Fraden, and Meyer [18]. First the equations are cast in a dimensionless form. The additional dimensionless variables needed are $z' = z/(\sqrt{2}l_c)$, and $v'_f = v_f/(\sqrt{2}l_c\omega)$. Equation (4.9) is solved using a forward finite difference method and Eq. (4.12) is solved using Gauss quadrature [19,20]. The equations are iterated at each time step until they converge.

Since detailed viscosity coefficients are not available for the NLC used by Migler and Meyer [11], the coefficients of 5*cb* found in the literature were used [21]. Hence, the comparison with experiment will be qualitative in nature.

V. VISCOSITY-REDUCTION LATTICE

We first attempt to simulate a VRL by using Eqs. (4.9) and (4.12) in the asynchronous regime in the presence of a disturbance that causes a local increase in viscosity. We find that near the disturbance there is a local increase in phase lag. This local nonhomogeneity in the director field gives rise to fluid flow. Further away, the fluid coupling is such that it creates a region of decreased effective viscosity so that there is a decreased phase lag relative to the homogeneous region. The ensuing dynamics is similar to the experimental observations given in Sec. III.

Figures 5 and 6 are results of a typical numerical simulation. In this case, the initial condition is a large-amplitude Gaussian peak of height π and width $x' = 10$. Similar results are obtained when α is initially homoge-

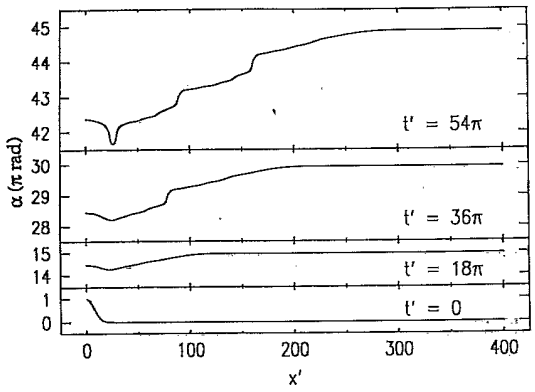

FIG. 5. Nucleation and growth of the viscosity-reduction lattice in the asynchronous regime, for $\omega\tau = 1.8$ and $(H')^2 = 110$. The initial condition (bottom plot) is a Gaussian function centered at the origin of height π. The homogeneous region is the flat part of the curves towards the right and the VRL is the growing disturbance on the left side. The value of α is greater in the homogeneous regime than in the VRL.

neous and there is a step-function increase in $\omega\tau$ in a narrow region near the origin. The reason for the Gaussian initial condition is that one can study the patterns as a function of $\omega\tau$ without worrying about the details of the disturbance. The only important piece of information we need to know about the disturbance is that at t'_{in}, it has created a local phase lag in the form of a Gaussian bump.

In Fig. 5, the time between plotted curves is long; $\Delta t' = 18\pi$, corresponding to 18 rotations of the field. The bottom plot shows the Gaussian initial condition. In the second plot, the nucleation of the VRL is evident to the right of the disturbance. In the next two plots, the VRL continues to grow, expanding into the initially homogeneous region. The homogeneous region (section of the curve toward the right which is relatively flat) has an increased phase-lag angle relative to the VRL, in agreement with experiment.

Figure 6 shows the dynamics within just two rotations of the field. Note that the behavior of $\alpha(x', t')$ is quite intricate. Roughly speaking, during one portion of the rotation, there are sharp wall-like structures propagating to the left. These are analogous to the dynamic solitons in the synchronous regime. In the other portion, the regions between the wall-like structures phase slip. Note that the overall shape of the structure is temporally periodic with the same frequency as the field rotation. Also, the lattice-homogeneous border has shifted over to the right, showing the growth of the lattice. These observations are in agreement with experiment.

Two basic properties of the lattice are its average wavelength λ' and the relative increase in its period relative to a homogeneous region,

$$\delta T = \frac{T_l - T_h}{T_h}, \tag{5.1}$$

i.e., the time for α in a VRL to increase by π, over that of a homogeneous region. These two quantities were measured in a growing lattice and so do not necessarily represent steady-state dynamic values. They are plotted as a function of H' with ω' held constant. (See Fig. 7.) As H' decreases, the wavelength increases strongly and $\delta T \to 0$ near the VRL-uniform transition, in qualitative agreement with the experimental findings [11]. The uniform regime corresponds to values of H' below this point, for which pattern formation is not observed. By searching for the point at which $\delta T \to 0$ as a function of ω', we can map out the VRL-uniform transition of the state diagram. This is shown in Fig. 8, and it is also in qualitative agreement with the experimental findings shown in Fig. 3.

In the above numerical integrations, we used as an initial condition a Gaussian bump of large amplitude. We note that for a given H' and ω', as the amplitude of the initial Gaussian function is decreased, one hits a point at which the VRL does not form and the director remains homogeneous. This is consistent with the experimental finding that a finite-sized disturbance is required to nucleate a VRL. All these results are dependent on the fluid-flow coupling. If this coupling is ignored, then an

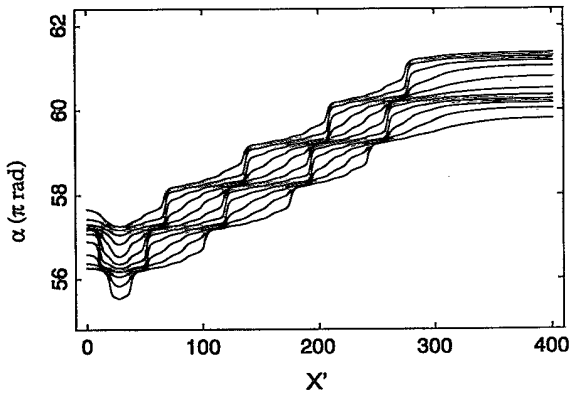

FIG. 6. Continuation of Fig. 5 but the time between plots is reduced, $\Delta t' = \pi/5$. The bottom plot corresponds to time $t' = 72\pi$.

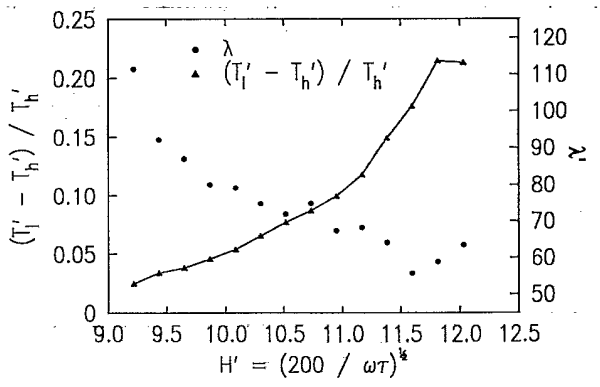

FIG. 7. Plot of the wavelength and period enhancement of the viscosity-reduction lattice, determined by numerical integration. At the right end, the wavelength seems to diverge.

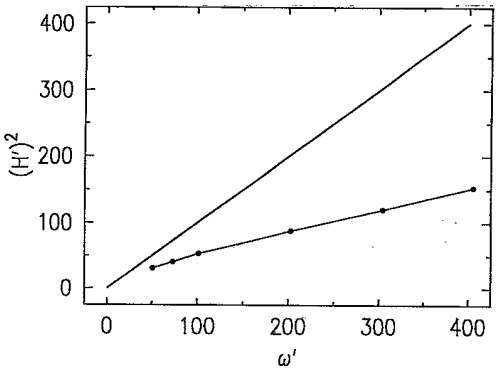

FIG. 8. Plot of the numerically determined transition between the VRL state (above the dotted line) and the uniform state. For reference, the synchronous-asynchronous transition is shown (solid line). Compare this to Fig. 3.

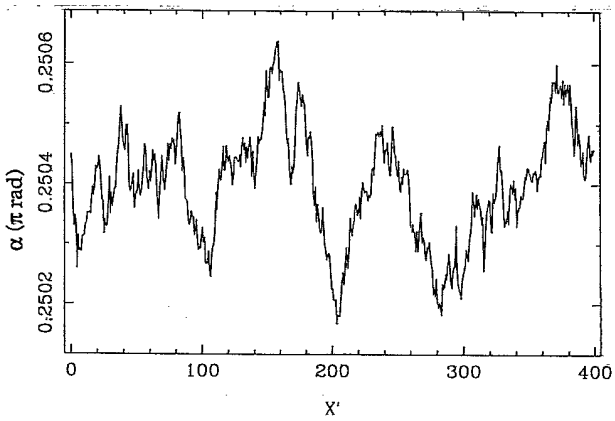

FIG. 9. Numerically generated thermal fluctuation.

initial Gaussian bump will not produce any of the above dynamics.

Thus we have shown several common features between the experimentally observed structures and those found numerically, suggesting that our model is correct. First is the fact that a growing dynamic structure is observed at all, with the property that α is an increasing function of distance from the nucleation point, a basic indication of viscosity reduction. Second is that the wavelength seems to diverge, along with a decrease in the magnitude of viscosity reduction, when the magnetic field is reduced towards the uniform state. Third, there is a complex time-dependent undulation of the local structure within the VRL, with period ω.

VI. AMPLIFIED THERMAL FLUCTUATIONS

In the *complex* part of the state diagram, an initially homogeneous sample will spontaneously become disordered. In this section, we will provide strong evidence that amplification of thermal fluctuations is the driving mechanism for the transition to this state. The amplification is caused by a director-fluid coupling. The *complex* state is an inherently two- (or three-) dimensional pattern. However, we can study the initial appearance of stripes during the first cycle of the director using our one-dimensional formalism.

The first question to address is the direction of the stripes. Experimentally, the system is free to select a direction for the stripes, while in the simulation, the wave vector is fixed along the x axis. From Eq. (4.9), we see that torque induced by flow gradients is largest when $\phi_{av} = 0$. From the above description of the stripes, we see that they are amplified when $\pi/4 < \alpha_{av} < 3\pi/4$. Thus it is reasonable to fix the initial conditions so that at the time of the cycle when $\phi_{av} = 0$ we have $\alpha_{av} = \pi/2$. The initial conditions are produced by the following procedure. First, α is initially set to $\pi/4$ because we find *numerically* that near this value thermal fluctuations begin to be amplified. Next for a given $\omega\tau$, using Eq. (2.9), we choose a starting time t'_{in} so that neglecting the thermal fluctuations, we will have $\phi = 0$ when $\alpha = \pi/2$. At this moment, the stripe wave vector will be parallel to the director. We add a random thermal fluctuation in α to the initial condition, shown in Fig. 9. The method used to generate the thermal fluctuation is well known and similar to that used by Srajer, Fraden, and Meyer [18].

Figure 10 shows the amplification and subsequent decay of a thermal fluctuation during the phase-slip portion of a single director cycle. One can clearly see the amplification of the fluctuation. We show only one cycle because, as discussed previously, the wave vector describing the next cycle of amplified thermal fluctuations has a different orientation, and the one-dimensional equations are not sufficient to describe this.

The maximum amplitude occurs for $\alpha_{av} \approx 3\pi/4$. In Fig. 11 we plot the maximum root-mean-square fluctuation as a function of $\omega\tau$ for different values of ω'. As $\omega\tau$ decreases, the magnitude of the fluctuations increases. This result is consistent with the experimental finding

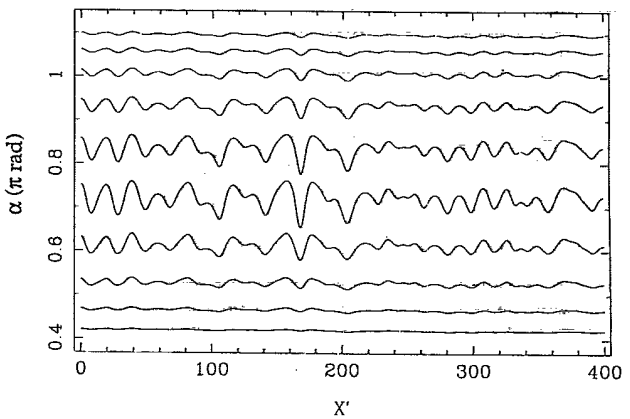

FIG. 10. Amplification of thermal fluctuations of Fig. 9 over a portion of the director cycle, for $\omega\tau = 1.2$, $(H')^2 = 90$.

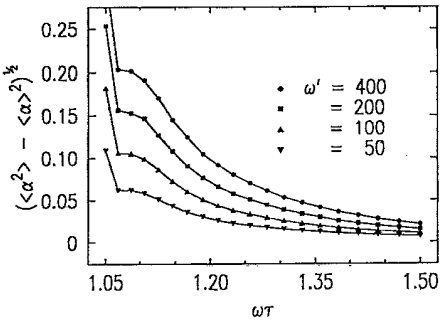

FIG. 11. The maximum rms amplitude for an amplified thermal fluctuation.

that for a given ω', the *complex* state occurs upon decreasing $\omega\tau$, and with the observation that the amplitude of the stripes increases with decreasing $\omega\tau$. We can estimate the size of the experimental fluctuations in the experiment as follows: since the contrast of the stripes is clearly visible between crossed polarizers, the order of magnitude of the peak-to-peak fluctuation is $\pi/8$. This is clearly in the range of the fluctuations seen in Fig. 11. However, there is no clear signal of when the amplified fluctuations would be strong enough to create the large-scale distortions seen in the *complex* state, as opposed to the transient stripes which appear in the VRL and VRL transverse instability that remain small. We did not probe in detail the jump that occurs in each plot for the smallest value of $\omega\tau$ since the experiments indicate that the *complex*-state can occur for much larger values of $\omega\tau$. We believe that the *complex*-state instability depends on subsequent cycles of the director and two-dimensional effects.

VII. CONCLUSION

In conclusion, we have explored by numerical studies how patterns develop from a sample that is initially homogeneous. The simulations confirm the experimental results that patterns may arise through either the amplification of thermal noise (complex state) or heterogeneous nucleations (VRL state). The pattern-forming states in the asynchronous regime share the feature that an inhomogeneous director pattern with fluid flow has a lower effective viscosity than a uniform director field and can respond more quickly to the driving magnetic field. We believe this is the important ingredient in understanding these states.

Now that we have confirmed that a set of one-dimensional equations of motion for the complex director and velocity fields reproduces the basic (one-dimensional) features of the asynchronous regime, one can attempt to arrive at a more analytical and more intuitive understanding of those features. We would like to understand the wavelength of the structures that appear, and why the VRL state grows by nucleation, while the complex state forms homogeneously by amplification of fluctuations. Beyond the one-dimensional model there are clearly many more unresolved questions.

ACKNOWLEDGMENTS

We wish to thank L. Abbot and T. Kepler for access to computer facilities and G. Kepler and G. Srajer for useful conversations. This research was supported by the National Science Foundation through Grant Nos. DMR-8803582 and DMR-9107013, and by the Martin Fisher School of Physics, Brandeis University.

* Present address: Exxon Research and Engineering Company, Route 22 East, Annandale, New Jersey 08801

[1] *Propagation in Systems far from Equilibrium*, edited by J. Wesfreid, H. Brand, P. Manneville, G. Albinet, and N. Boccara (Springer-Verlag, Berlin, 1988).
[2] *Oscillations and Traveling Waves in Chemical Systems*, edited by R.J. Field and M. Burger (Wiley, New York, 1985).
[3] *Solitons in Liquid Crystals*, edited by L. Lam and J. Prost (Springer-Verlag, Berlin, in press).
[4] P.G. de Gennes, *The Physics of Liquid Crystals* (Clarendon, Oxford, 1975).
[5] See, for example, A. Joets, X.D. Yang, and R. Ribotta, Physica D **23D**, 235 (1986); W. Thom, W. Zimmermann, and L. Kramer, Liq. Cryst. **4**, 309 (1989); Ingo Rehberg, Steffen Rasenat, and Victor Steinberg, Phys. Rev. Lett. **62**, 756 (1989).
[6] P. Pieranski and E. Guyon, Phys. Rev. Lett. **39**, 1280 (1977); E. Dubois-Violette and F. Rothen, J. Phys. (Paris) **39**, 1039 (1978); E. Guazzeli and E. Guyon, *ibid.* **43**, 985 (1982).
[7] F. Brochard, P. Pieranski, and E. Guyon, Phys. Rev. Lett. **28**, 1681 (1972).
[8] E.F. Carr, Mol. Cryst. Liq. Cryst. **34**, 159 (1977).
[9] E. Guyon, R. Meyer, and J. Salan, Mol. Cryst. Liq. Cryst. **54**, 261 (1979).
[10] B. L. Winkler *et al.*, Phys. Rev. A **43**, 1940 (1991).
[11] K. Migler and R. Meyer, Phys. Rev. Lett. **66**, 1485 (1991).
[12] F. Brochard, L. Léger, and R.B. Meyer, J. Phys. (Paris) **36**, Suppl. C1, 209 (1975).
[13] F. Brochard, J. Phys. (Paris) Lett. **35**, L19 (1974).
[14] F. Sagués, Phys. Rev. A **38**, 5360 (1988).
[15] F. Brochard, Ph.D. thesis, Université Paris–Sud, Orsay (1974) (unpublished).
[16] M. Buttiker and R. Landauer, Phys. Rev. A **23**, 1397 (1981).
[17] F. Lonberg, S. Fraden, A.J. Hurd, and R.B. Meyer, Phys. Rev. Lett. **52**, 1903 (1984).
[18] G. Srajer, S. Fraden, and R.B. Meyer, Phys. Rev. A **39**, 4828 (1989), and references therein.
[19] H. Ferziger, *Numerical Methods for Engineering Application* (Wiley, New York, 1981).
[20] W.H. Press, B.P. Flannery, S. Teukolsky, and W.T. Vetterling, *Numerical Recipes* (Cambridge University Press, Cambridge, England, 1985).
[21] W.H. de Jeu, *Physical Properties of Liquid Crystal Materials* (Gordon and Breach, New York, 1980).